



# A new mini-triaxial cell for combined high-pressure and high-temperature *in situ* synchrotron X-ray microtomography experiments up to 400°C and 24 MPa

Marco Voltolini,<sup>a\*</sup> Harold Barnard,<sup>b</sup> Patrice Creux<sup>c</sup> and Jonathan Ajo-Franklin<sup>a</sup>

Received 22 August 2018

Accepted 4 November 2018

Edited by A. Momose, Tohoku University, Japan

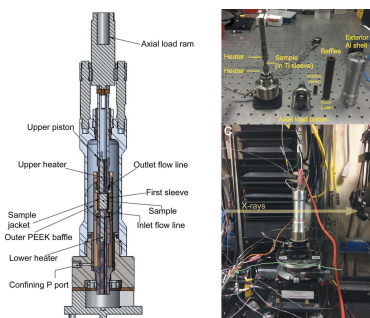
**Keywords:** X-ray micro-tomography; high pressure and temperature; *in situ* X-ray imaging; earth sciences.

<sup>a</sup>Earth and Environmental Sciences Area, Energy Geoscience Division, Lawrence Berkeley National Laboratory, 1 Cyclotron Road, Berkeley, CA 94720, USA, <sup>b</sup>Advanced Light Source, Lawrence Berkeley National Laboratory, 1 Cyclotron Road, Berkeley, CA 94720, USA, and <sup>c</sup>Laboratoire des Fluides Complexes et leurs Réservoirs – IPRA, UMR5150, CNRS/TOTAL/Univ Pau and Pays Adour, Pau 64000, France. \*Correspondence e-mail: mvoltolini@lbl.gov

A new experimental triaxial cell for *in situ* synchrotron X-ray micro-computed tomography aimed at imaging small samples (6 mm × 19 mm) at high temperatures (up to 400°C) and pressures (up to 24 MPa confining) is presented. The system has flow-through capabilities, independent axial and radial pressure control, and has been developed and tested at the 8.3.2. beamline at the Advanced Light Source. The characteristics of this new experimental rig are described, along with the challenges, mainly concerning the combination of X-ray transparency with vessel strength at high temperature, and solutions found during the development stage. An experiment involving oil shale pyrolysis under subsurface conditions, highlighting the importance of a device able to operate in this pressure and temperature range, is also introduced. The availability of this cell enables an unprecedented range of experiments in the Earth Sciences, with a special focus on subsurface geothermal processes.

## 1. Introduction

X-ray micro-computed tomography (XR $\mu$ CT), using either conventional or synchrotron X-ray sources, is an established experimental technique in the geosciences which provides useful 3D (or 4D, in the case of dynamic systems) visualization capability in a non-destructive fashion, thus enabling the study of a large variety of phenomena at micrometre resolution [see Gualda *et al.* (2010) and Cnudde & Boone (2013) for general reviews]. The success of the technique is due to several factors, beyond the simple 3D visualization. XR $\mu$ CT data can be used to describe the sample microstructure in a quantitative fashion via morphometric analysis, and several dedicated software packages are available, both commercial (*e.g.* Avizo, Visualization Science Group; Dragonfly, Object Research System) or developed by research institutes [*e.g.* iMorph (Brun & Camille, 2009); Pore3D (Brun *et al.*, 2010)]. More recently, the concept of digital rock physics has led to the development of software tools able to replicate experiments aimed at computationally measuring physical properties of materials using XR $\mu$ CT datasets. Properties modeled to date include elastic moduli (Madonna *et al.*, 2012), mercury intrusion porosimetry and drainage curves (Voltolini *et al.*, 2017a), permeability and electrical conductivity (Andrä *et al.*, 2013), and gas flow dynamics (Degruyter *et al.*, 2010), opening new opportunities for geoscientists to better understand the role of morphological features in controlling specific physical properties.



The availability of high-brilliance X-ray sources such as synchrotrons, coupled with *in situ* environmental cells, facilitates 4D XR $\mu$ CT experiments, where the evolution of the sample is monitored in time as external parameters are varied. The *in situ* cells built for SXR $\mu$ CT experiments can often control several variables of interest to the geoscientist: samples can be imaged when, for example, subjected to variations in stress state, temperature or reactive flow. A series of five such examples relevant to the earth sciences utilizing different environmental cells was presented by Voltolini *et al.* (2017b). When considering subsurface processes, two main variables are usually considered: pressure and temperature. In general, *in situ* cells for XR $\mu$ CT consider large variations for only one of these parameters, since either heating or compressing a sample often requires a comparatively simple setup. This segment of cells is often focused towards the extremes, *e.g.* very high temperatures, which is of interest mostly for volcanologists (Baker *et al.*, 2012; Godinho *et al.*, 2016). Pressure-only experimental rigs (uniaxial and triaxial) are often used in testing mechanical properties of different materials (*e.g.* Buffiere *et al.*, 2010). A third important parameter concerning the subsurface environment is transport: reactive and unreactive flow in rocks is usually studied at room temperature, with or without pressurization.

While flow experiments at both ambient pressure ( $P$ ) and temperature ( $T$ ) can be attained with a relatively simple cell, adding confinement and pore fluid pressures requires more specialized cells. A few research groups have developed such *in situ* cells: a simple low- $P$  cell for reactive transport was shown by Voltolini *et al.* (2017b), and room- or low-temperature cells able to operate at high pressure ('high' intended as tens of MPa) for flow have been developed to be used at different synchrotron beamlines (*e.g.* Menke *et al.*, 2015; Al-Khulaifi *et al.*, 2017; Voltolini *et al.*, 2017a). Cells with confining pressure have also been used for rock deformation experiments at room temperature with varying levels of confining and pore pressures (*e.g.* Desrues *et al.*, 1996; Viggiani *et al.*, 2004; Renard *et al.*, 2009). Cells combining high pressure and temperature exist (Fusseis *et al.*, 2014), but temperature control is often limited to  $\sim 200^\circ\text{C}$  because of material constraints, even if a cell able to operate at significantly high pressure (Renard *et al.*, 2016) and slightly higher temperature (claimed at  $250^\circ\text{C}$  maximum) has been developed. For extreme high temperatures and pressures, Drickamer-type cells have been employed (Wang *et al.*, 2005), with all the limitations intrinsic to these setups (heavy and bulky, limited sample size, issues with sample rotation, flow, *etc.*).

A mini-triaxial XR $\mu$ CT cell breaking the limit of  $200^\circ\text{C}$  and going up to  $400^\circ\text{C}$  allows the investigation of processes over the whole hydrothermal temperature (and pressure) range, conditions not currently accessible in this context. This  $P/T$  interval is increasing in importance because of the recent geothermal energy impulse, and a significant range of mineralization processes important for the industry occur in this range as well. Additionally, geochemical reactions too slow to be observed with *in situ* measurements can have their reaction rates boosted by an increase in temperature.

In this work we will describe such a cell, tested to  $400^\circ\text{C}$  and 24 MPa, confining stress, and discuss the solutions employed to solve the various issues encountered during the development. We will also present a preliminary experiment demonstrating the utility of a cell, targeting oil shale pyrolysis.

## 2. Description of the apparatus

The most immediate challenge faced in developing an XR $\mu$ CT compatible triaxial cell able to operate at high temperature and high pressure (HT/HP) is the requirement of using materials able to both maintain their mechanical properties at high temperature and have low X-ray attenuation. Unfortunately, the aluminium alloys used for many prior XR $\mu$ CT *in situ* cells (Al 6061/7075) rapidly lose tensile strength at temperatures above  $150^\circ\text{C}$ , making such designs problematic. Many alloys designed for higher temperatures are insufficiently transparent in the energy range available at our facility. This limitation is especially critical when considering designs where the whole cell assembly is heated, so we opted for a design where the heating is localized as close as possible to the sample. This approach, augmented by the use of an insulating baffle, allowed use of low-temperature Al alloys for the outer shell of the cell while achieving our target temperature and stress conditions on the sample. Due to the large surface area of the vessel and the small zone where heat is generated and transferred on the sample, external air cooling is sufficient to maintain a large thermal gradient.

The full apparatus was built for integration into beamline 8.3.2 at the Advanced Light Source (ALS) synchrotron, at the Lawrence Berkeley National Laboratory. The system is composed of a pressure control sub-system with three high-pressure syringe pumps and associated plumbing, a temperature controller for the heating system of the cell, and the cell main body. The three pumps are reduced-height versions of 260HP Teledyne Isco pumps, customized for available space in the experimental hutch, and are connected to the cell via 1/16-inch stainless steel tubing. Pumps have been shortened to a height of  $\sim 70$  cm, with the result of decreasing the available volume of fluids to store in the cylinder to  $\sim 100$  cc. Two main configurations are available with this three-pump system: (1) the first pump controls the lateral confining pressure, the second one controls the axial load, and the third one controls the pore pressure, all working in constant pressure mode; (2) the first pump is connected to both axial and lateral confining pressure lines, the second is connected to the sample in constant flow mode, the third is connected to the opposite end of the sample and sets the pore pressure. Configuration (1) is used for experiments requiring biaxial differential pressure (*e.g.* rock deformation), while configuration (2) typically targets reactive flow experiments (weathering, mineralization, *etc.*).

This flexibility of the system allows for a large range of experiments to be performed. The cell itself is a mini-triaxial vessel (co-designed with Coretest Systems, Morgan Hill, CA, USA), and conceptually derived from the cell presented by

Voltolini *et al.* (2017a). In Fig. 1(a) a schematic of the cell is displayed. Fig. 1(b) shows the cell partially dismantled, to highlight the inner baffles system. In Fig. 1(c) the cell deployed at the beamline during the first experiment is shown. The high-temperature cell is built to host cylindrical samples of diameter 6.35 mm, up to 19 mm tall, and the upper and lower stainless steel pistons are sized accordingly. Each piston accommodates a slot for a 50 W heating cartridge, two thermocouple (J-type) slots, and a flow line. On the top of the upper piston, a pressure-driven ram connected to the pump systems provides the axial load. The top assembly also houses a support bracket connected to the piston and a clamp to allow a linear variable differential transformer device (connected to a computer outside the hutch) to be mounted, thus enabling the measurement and recording of the vertical strain in real time during the experiments.

The cylindrical sample is confined by a thin metal jacket (either titanium grade 5 or annealed copper) connected to the pistons endplugs with conical compression nuts. The sample jacket is surrounded by the inner PEEK or Vespel sleeve, acting as the first thermal insulator. The whole sample assembly is again surrounded by a second PEEK or Vespel sleeve to create a baffle system to prevent thermal loss from the sample. This assembly is encapsulated in an aluminium (7075-T651) pressure vessel providing the enclosure for the lateral confinement medium, in this case inert gas (N<sub>2</sub>). This

outer shell is threaded to the stainless steel bottom of the body, and a top gland nut system with a Kalrez O-ring seals the connection with the upper axial piston. The two heating cartridges are controlled by a programmable temperature controller (PTC10, Stanford Research Systems) with J-type thermocouples monitoring the upper and lower piston, and a K-type thermocouple monitoring the temperature of the outer shell, which is actively cooled by a fan system inside of the hutch. The two plastic baffle systems set in the space between the sample and the outer aluminium shell efficiently decrease heat transfer.

As mentioned previously, the choice of suitable materials was challenging and several problems needed to be addressed simultaneously: especially for the outer shell, the ideal building material needs to be both X-ray transparent at the energies available at 8.3.2 (at the sample level) and maintain proper mechanical properties to withstand the pressurization while at 400°C; concerning the X-ray attenuation issue versus mechanical strength, the discussion for the cell presented in Fig. 1 of Voltolini *et al.* (2017a) is still valid but with the non-trivial addition of the temperature issue. Given the X-ray spectrum at 8.3.2 when using filtered white light, peaking at ~30 keV of X-ray energy, the use of dense materials such as those found with the titanium shell presented by Renard *et al.* (2016), aimed at a beamline with significantly harder X-rays, has to be excluded. From the X-ray transparency point of view,

plastics are the ideal material, but the polymer with the best mechanical properties at high temperature, Kalrez, is rated up to 327°C. It has been used only for the seal on the upper piston, where the temperature is higher and the mechanical properties are not essential. Vespel has a slightly lower temperature performance, and it has been chosen for the first sleeve around the sample jacket. Other materials that can be considered for the outer shell are beryllium alloys, which pose significant safety issues related to Be toxicity. Aluminium alloys provide good X-ray transparency, good mechanical properties and excellent machining characteristics; unfortunately, the mechanical properties of most aluminium alloys tend to degrade above ~150°C where irreversible modifications in the alloy microstructure start to occur (*e.g.* Summers *et al.*, 2015). Except for this last issue, aluminium was the best candidate, therefore we built the outer shell out of 7075-T651 alloy and engineered a system to avoid the shell reaching above ~100°C in temperature. Since thermal damage is cumulative, operation of the vessel requires careful

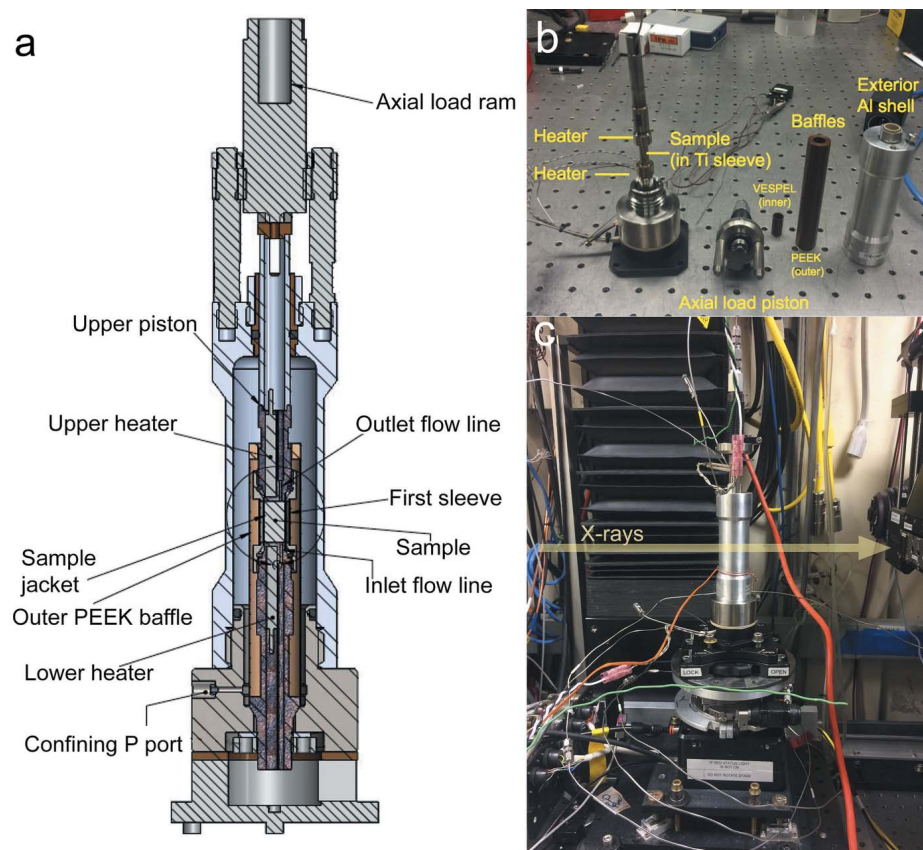


**Figure 1**  
 (a) Section of the schematics of the HP/HT cell. (b) The partially dismantled cell, showing the baffle system used to slow heat transfer down. (c) The cell mounted on the rotating stage at the 8.3.2 beamline at the ALS during the first experimental run.

monitoring of shell temperature to ensure safe long-term operations.

An active cooling system through an electric fan provides cooling for the outer shell; the baffle system ensures that this cooling only marginally affects the sample, which should be kept at high temperature. The whole cell has been designed to both minimize heat transfer from the pistons and sample to the outer cell to protect the aluminium shell, and to slow thermal diffusion in order to obtain a faster and more homogeneous heating of the sample itself. Another problem arises when considering the confining pressure medium: in triaxial cells pressure media are usually low-compressibility fluids, typically water or oil. These fluids are not suitable for operation at 400°C, therefore we decided to use inert gas (N<sub>2</sub>). Gas pressurization has the advantage of lower thermal conductivity, and has lower X-ray attenuation as well, but it stores a much larger amount of energy when compressed and heated, generating safety concerns in case of failure of the cell. To provide a secondary measure of operator safety, a polycarbonate blast shield was installed for all high-temperature experiments.

An additional critical issue for the cell was the choice of the sample jacket: plastics and elastomers cannot be used at 400°C, so thin (~100 µm) titanium sleeves were tested. These sleeves perform well, but are extremely stiff, making deformation experiments difficult, with the sleeve strength dominating the system. To overcome this problem, we machined copper sleeves of similar thickness. Different problems arose from the use of thin copper sleeves: while they are temperature resistant and mechanically soft, allowing to conform and adapt to the sample during pressurization and deformation, their higher X-ray attenuation decreases the quality of the images, and they are more prone to puncturing issues (leaks), as well as being more chemically reactive.

A filler material, such as graphite powder with a very small amount of high-temperature epoxy used as a binding agent, or thin carbon composites sheets, were generally used with the stiff jackets to fill the sample-jacket gap. The combination of these materials provides an adequate X-ray transparency at the sample level, while allowing safe operation at the highest temperature. The main problem related to image quality with the current setup is the presence of a highly attenuating sample jacket: the quality rapidly decreases close to the outer rim of the sample, because of the increasing length of the path the X-rays need to go through the dense jacket. This issue is effectively minimized by adding a thin layer (~100 µm thick) of more X-ray transparent filler material to avoid having the sample in direct contact with the jacket, since in the radiograph the path of the X-rays passing through the jacket material increases approximately exponentially from the center of the sample going laterally towards the inner surface of the jacket; even such a thin layer of material significantly increases the overall data quality.

The maximum temperature this system can reach, and was also tested in actual experiments, is 400°C. Pressure-wise our system has been successfully tested up to 15 MPa, but it has been built to reach 24 MPa, with flow capabilities.

### 2.1. Use at the 8.3.2 beamline at ALS

As mentioned in the previous discussion, the experimental system was tailored to the 8.3.2 beamline at the ALS (MacDowell *et al.*, 2012). The three high-pressure pumps have been modified to fit underneath the optics table in the experimental hutch, allowing a rapid deployment of the whole system, set on carts. The temperature controller is placed outside, so the temperature can be monitored and varied without the need of opening and closing the hutch. Given the spectrum of the X-ray beam from the insertion device, the cell is intended to be operated using filtered white light, with a 6 mm in-line aluminium filter, and a 0.5 mm copper filter placed before the cell. The general sample size was chosen because of the compromise between resolution and field of view (FOV); this specific sample size was chosen to be optimal with the following optics system available at the beamline: 500 µm Ce-doped LuAG scintillator (Crytur), 2× Mitutoyo objective lenses with long working distance (0.055 numerical aperture), pco.edge 2560 pixel × 2160 pixel sCMOS detector, resulting in a pixel size of 3.22 µm with a lateral FOV of 8.24 mm, allowing for a full-field tomography of the sample, including jacket and some eventual bulging due to deformation, to obtain the full set of boundary conditions in case modeling with the data is required. Vertical FOV is limited by the X-ray beam vertical size and is ~4.5 mm. The system has also been successfully tested with 5× optics in a ‘local area’ setup, with a resulting 1.29 µm pixel size and 3.3 mm FOV. A high-quality single volume (vertical stacking of multiple volumes is required for taller samples) with 1025 projections in continuous tomography is collected in ~2 min, making the data collection of the tallest possible sample last ~15 min. Scanning time can be significantly reduced using the available pco.dimax camera, at the expense of image quality (increased signal-to-noise ratio), in case of fast evolving systems.

### 3. Oil shale artificial maturation at subsurface pressure conditions

As an application example, we show the main results from an experiment involving Green River oil shale confined pyrolysis. This class of experiments is critical to improve understanding of both natural and artificial (*i.e.* induced by heating) oil shale maturation (Moyer & Prasad, 2017), particularly the presence, absence and connectivity of thermomechanically induced fractures or cracks. Previous experiments examining oil shale pyrolysis have been carried out without confinement, and a fracture network development was observed (Panahi *et al.*, 2014; Saif *et al.*, 2016). Results from unconfined experiments are challenging to extend to reservoir conditions, where the *in situ* stress field plays an important role.

In this experiment a semi-rigid titanium jacket was used. The sample was heated to 375°C, with application of 13.8 MPa of confining pressure (both axial and lateral) and 5.5 MPa of pore pressure; such a large difference was selected to evaluate the deformation of the titanium jacket. The experiment shows that the oil shale at high temperature and pressure displays

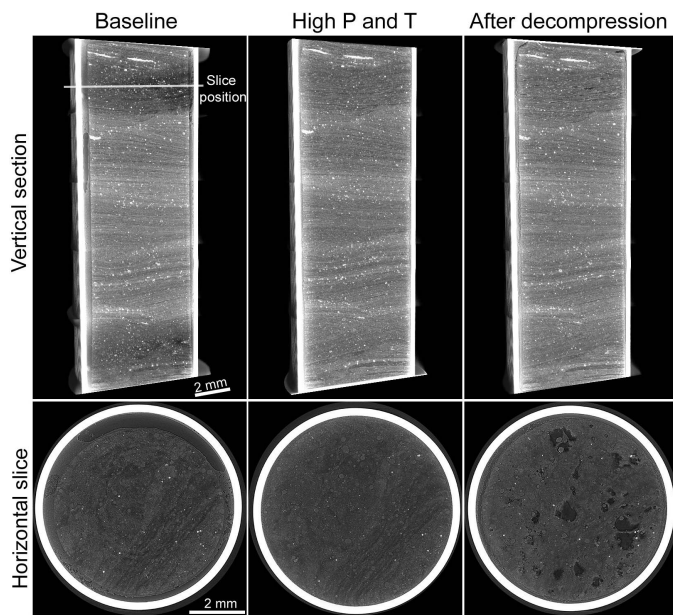


**Figure 2**  
The evolution of the oil shale sample used during one of the experiments: on the top row the volume rendering of vertical sections of the whole sample are shown for the sample at ambient temperature ('Baseline'), at 13.8 MPa of confining pressure and 5.5 MPa of pore pressure at 375°C ('High P and T'), and after depressurizing and cooling the sample ('After decompression'). In the bottom row, equivalent horizontal slices from the top part of the sample (as marked in figure) are displayed.

a markedly plastic behavior with no fracturing. Fracturing is observed during depressurization and cooling, and at this stage the sample microstructure closely resembles those observed in unconfined experiments previously cited. In Fig. 2 (top) a vertical section of the whole sample is shown for three different stages: baseline (room temperature), the sample after maximum pressurization and heating, and finally the sample after depressurizing and venting the cell. In Fig. 2 (bottom) three matching horizontal slices of the sample are shown to highlight both the behavior of the sample and the high quality of the data collected. As can be seen, thermal expansion and some localized plastic flow can be seen in the HPT/HT panel (center section), particularly at the top of the sample. The fractures generated during depressurization, presumably by gas exsolution, are visible in an organic-rich layer in the right panel.

#### 4. Conclusions

We have presented a new environmental cell aimed at *in situ* SXR $\mu$ CT measurements in an unprecedented range of combined pressure and temperature, with flow capabilities. The FOV/resolution range makes it suitable for a large number of experiments in very different fields. In the Earth Sciences, this cell enables experiments targeted to high-temperature processes in the subsurface. While temperatures related to volcanology and deep crustal deformation cannot be reached, with operations up to 400°C the whole geothermal temperature spectrum becomes accessible, making new

experiments probing high-temperature dissolution, mineralization, induced seismicity and thermomechanical fracturing possible. As an example application we show preliminary results from an oil shale pyrolysis experiment which leverages the HP/HT performance of the cell; the pronounced differences between the confined and unconfined experiments show that any interpretation of this process from unconfined experiments cannot be extended to the subsurface, hence the necessity of this new class of experimental devices.

#### Acknowledgements

Dula Parkinson and the staff at 8.3.2 are acknowledged for their help during the measurements at the ALS. Alexandre Lapene is acknowledged for useful discussion.

#### Funding information

The following funding is acknowledged: Total SA supported the development of the experimental cell. The Advanced Light Source is supported by the Director, Office of Science, Office of Basic Energy Sciences, of the US Department of Energy (award No. DE-AC02-05CH11231).

#### References

Al-Khulaifi, Y., Lin, Q., Blunt, M. J. & Bijeljic, B. (2017). *Environ. Sci. Technol.* **51**, 4108–4116.  
 Andr a, H., Combaret, N., Dvorkin, J., Glatt, E., Han, J., Kabel, M., Keehm, Y., Krzikalla, F., Lee, M., Madonna, C., Marsh, M., Mukerji, T., Saenger, E. H., Sain, R., Saxena, N., Ricker, S., Wiegmann, A. & Zhan, X. (2013). *Comput. Geosci.* **50**, 33–43.  
 Baker, D. R., Brun, F., O'Shaughnessy, C., Mancini, L., Fife, J. L. & Rivers, M. (2012). *Nat. Commun.* **3**, 1135.  
 Brun, E. & Camille, M. (2009). Doctoral dissertation, Aix-Marseille 1, France.  
 Brun, F., Mancini, L., Kasae, P., Favretto, S., Dreossi, D. & Tromba, G. (2010). *Nucl. Instrum. Methods Phys. Res. A*, **615**, 326–332.  
 Buffiere, J. Y., Maire, E., Adrien, J., Masse, J. P. & Boller, E. (2010). *Exp. Mech.* **50**, 289–305.  
 Cnudde, V. & Boone, M. N. (2013). *Earth Sci. Rev.* **123**, 1–17.  
 Degruyter, W., Burgisser, A., Bachmann, O. & Malaspinas, O. (2010). *Geosphere*, **6**, 470–481.  
 Desrues, J., Chambon, R., Mokni, M. & Mazerolle, F. (1996). *G eotechnique*, **46**, 529–546.  
 Fusses, F., Steeb, H., Xiao, X., Zhu, W., Butler, I. B., Elphick, S. & M ader, U. (2014). *J. Synchrotron Rad.* **21**, 251–253.  
 Godinho, J., Lee, P., Lavalley, Y., Kendrick, J. & Von-Aulock, F. (2016). *EGU Gen. Assembly Conf. Abstr.* **18**, 14369.  
 Gualda, G. A., Baker, D. R. & Polacci, M. (2010). *Geosphere*, **6**, 468–469.  
 MacDowell, A. A., Parkinson, D. Y., Haboub, A., Schaible, E., Nasiatka, J. R., Yee, C. A., Jameson, J. R., Ajo-Franklin, J. B., Brodersen, C. R. & McElrone, A. J. (2012). *Proc. SPIE*, **8506**, 850618.  
 Madonna, C., Almqvist, B. S. & Saenger, E. H. (2012). *Geophys. J. Int.* **189**, 1475–1482.  
 Menke, H. P., Bijeljic, B., Andrew, M. G. & Blunt, M. J. (2015). *Environ. Sci. Technol.* **49**, 4407–4414.  
 Moyer, J. & Prasad, M. (2017). *Geophysics*, **82**, MR175–MR190.  
 Panahi, H., Mazzini, A., Jamtveit, B., Kobchenko, M., Dysthe, D. K., Renard, F., Meakin, P., Malthe-S orensen, A. & Scheibert, J. (2014). *SPE J.* **18**, 366–377.  
 Renard, F., Bernard, D., Desrues, J. & Ougier-Simonin, A. (2009). *Earth Planet. Sci. Lett.* **286**(1–2), 285–291.

- Renard, F., Cordonnier, B., Dysthe, D. K., Boller, E., Tafforeau, P. & Rack, A. (2016). *J. Synchrotron Rad.* **23**, 1030–1034.
- Saif, T., Lin, Q., Singh, K., Bijeljic, B. & Blunt, M. J. (2016). *Geophys. Res. Lett.* **43**, 6799–6807.
- Summers, P. T., Chen, Y., Rippe, C. M., Allen, B., Mouritz, A. P., Case, S. W. & Lattimer, B. Y. (2015). *Fire Sci. Rev.* **4**, 3(1–36).
- Viggiani, G., Lenoir, N., Bésuelle, P., Di Michiel, M., Marelllo, S., Desrués, J. & Kretschmer, M. (2004). *C. R. MéCan.* **332**, 819–826.
- Voltolini, M., Haboub, A., Dou, S., Kwon, T.-H., MacDowell, A. A., Parkinson, D. Y. & Ajo-Franklin, J. (2017b). *J. Synchrotron Rad.* **24**, 1237–1249.
- Voltolini, M., Kwon, T. H. & Ajo-Franklin, J. (2017a). *Int. J. Greenhouse Gas Control*, **66**, 230–245.
- Wang, Y., Uchida, T., Westferro, F., Rivers, M. L., Nishiyama, N., Gebhardt, J., Leshner, C. E. & Sutton, S. R. (2005). *Rev. Sci. Instrum.* **76**, 073709.